Chapter 6

Enhanced Thermal Stability and Catalytic Performance of Montmorillonite-Silica-Graphene Oxide Composite Incorporating with Chiral Thiourea for the Strecker Reaction

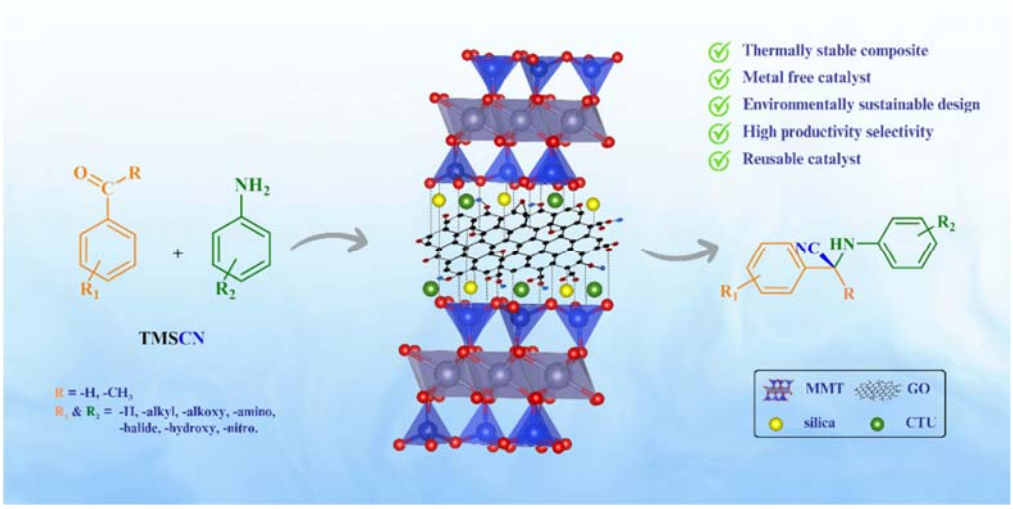

6.1 Introduction

The development of efficient and selective catalysts is crucial for various chemical reactions in industrial processes. Catalysts can increase the reaction rate, reduce energy consumption, and improve the selectivity of the desired products.[1,2] Over the years, substantial development has been made in the advancement of new catalytic systems, and among them, heterogeneous catalysts have gained significant attention due to their advantages over homogeneous catalysts, such as easy separation, reusability, and stability.[3,4] Montmorillonite, silica and graphene oxide are commonly used support materials for heterogeneous systems due to their unique chemical and physical characteristics.[5] Montmorillonite (MMT) is a naturally occurring clay mineral that has a layered structure and a large surface area, making it an excellent support material for catalytic applications.[6,7] However, at higher temperatures, MMT loses its catalytic active sites due to its low thermal stability, which limits its applications in catalytic activity.[8] Silica is another widely used support material due to its thermal stability, mechanical strength, and high surface area.[9–11] Graphene oxide (GO) has garnered substantial attention in recent years due to its distinctive physical and chemical properties, including a high surface area and exceptional mechanical properties.[12] These properties make GO a promising candidate for catalytic applications. However, the low dispersion and aggregation of GO in solution limits its practical applications as a catalyst. [13]

To address this issue, the present work has the capability to overcome it, including the combination of these support materials to form a composite material that improves thermal stability compared to MMT and GO and produces a synergistic effect, which can enhance the catalytic activity and selectivity of the composite material. Therefore, the development of MMT-silica-GO composite is of significant interest to the scientific community and has potential industrial applications.

Furthermore, the synthesized chiral thiourea-based (CTU) moiety was incorporated into the MMT-silica-GO-based composite and evaluated for its catalytic performance in the Strecker reaction. Researchers have used thiourea-based scaffolds as catalysts for various chemical reactions, including the Strecker reaction.[14] These reactions were typically catalyzed by Lewis

acid-base catalysts.[15] The recovery and recycling of the organocatalyst can, however, be challenging in homogeneous mode. To address this issue, researchers have explored the use of metal-based complexes as heterogeneous catalysts, offering easy separation and reusability. However, this technique is also associated with metal leaching.[16,17] This is where the metal catalyst can dissolve or disperse into the reaction mixture, causing potential contamination and a loss of catalyst activity.[18,19] Therefore, there is significant potential to develop a novel class of catalysts that operate efficiently under mild conditions, using fewer toxic solvents or even metal-free systems. These catalysts would require lower catalytic loading while still achieving high conversion rates. This approach would not only address metal leaching concerns but also contribute to greener and more sustainable catalytic processes.[20–22] While incorporating thiourea-based scaffolds into the MMT-silica-GO-based composite is expected to improve its stability and reusability. In this work, we report a heterogenous organocatalyst, MMT-silica-GO-CTU, containing an amino acid-based asymmetric scaffold, as shown in *Scheme 6.1*. The present catalyst was tested for the Strecker reaction. It has been found to be highly effective in facilitating the conversion of various aldehydes and ketones into α-aminonitriles under the mild reaction conditions. A major feature of this catalyst is its excellent recyclability, which enables it to remain active even after five cycles in use.

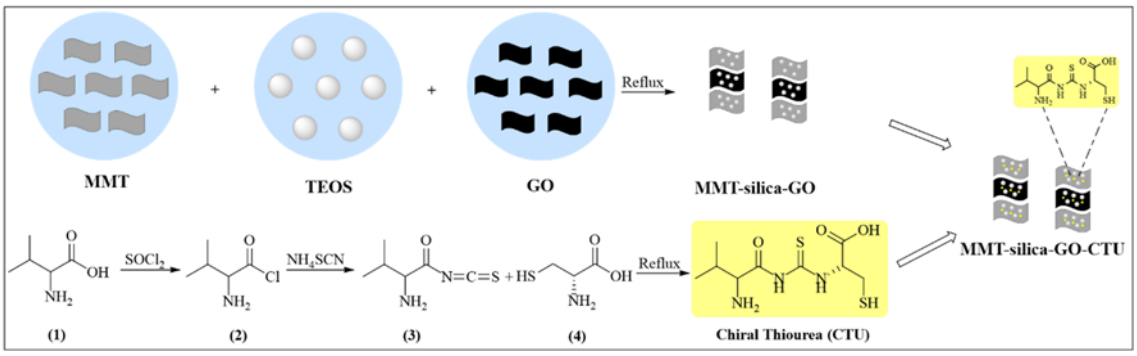

Scheme 6.1 A state-of-the-art pathway for synthesizing MMT-silica-GO-CTU.

6.2 Experimental Section

Montmorillonite K10 and natural flake graphite with a particle size smaller than 20 μm and a purity of 99.95% were procured from Sigma Aldrich. *dl*-Valine, D-cysteine, and TEOS were acquired from TCI Pvt. Ltd. Additional chemicals were obtained from S D Fine Chem Ltd. All the chemicals and solvents used in the synthesis were commercially sourced and used without further purification.

6.2.1 Preparation of Graphene oxide (GO)

Graphene oxide was synthesized using a modified version of the Hummer's method.[23–25]

6.2.2 Preparation of MMT-silica-GO

The MMT-silica-GO composite was synthesized using a sol-gel method. Initially, GO (0.25 g) and MMT (2.5 g) were separately dispersed in a 350 ml EtOH:H_2O solution (5:1, v/v) using ultrasonication for 30 minutes. Subsequently, a solution containing 3 mL of TEOS and 10 mL of ammonia was stirred on a magnetic stirrer. The dispersion solution of graphene oxide (GO) and montmorillonite (MMT) was added dropwise to the reaction mixture, followed by stirring for 10 h at 80°C. Once the reaction was complete, the mixture underwent centrifugation and was washed multiple times using H_2O and EtOH. The resulting product was then dried under vacuum at 70°C for 5 h.[26–28]

6.2.3 General synthesis of chiral thiourea (CTU)

Valinoyl chloride was synthesized through a traditional acylation reaction between *dl*-valine and thionyl chloride, following a reported method. Valinoyl isothiocyanate was then synthesized from valinoyl chloride and ammonium thiocyanate, based on literature procedures. The light yellowish solution obtained after filtration was directly used in the subsequent step without undergoing any additional purification steps. In the subsequent step, a solution of valinoyl isothiocyanate in acetone was prepared. Subsequently, *d*-cysteine in acetone (3 ml) was added

dropwise to the reaction mixture. Then reaction mixture was refluxed for 12 h. Once the reaction was determined to have reached completion, the solution was cooled to room temperature and subsequently poured into a beaker containing cracked ice. The subsequent precipitate was filtered and thoroughly washed with H_2O. Finally, the precipitate was dried under vacuum.[29–32]

6.2.4 Preparation of MMT-silica-GO composite encapsulated with chiral thiourea-based moiety (MMT-silica-GO-CTU)

The MMT-silica-GO composite (0.25 mg) was mixed thoroughly with an excess of chiral thiourea-based moiety. The mixture was covered with an appropriate amount of solvent. Subsequently, the flask was sealed, and the mixture was refluxed for 24 h under a inert gas flow. Any unreacted moiety was extracted using acetone. The resulting sample was washed extensively with a volatile solvent and then dried in an air oven for 60 minutes. This process yielded the MMT-silica-GO composite encapsulated with the chiral thiourea-based moiety (as illustrated in *Scheme 6.1*).

6.2.5 General condition for the catalytic reaction

In a typical reaction, a mixture containing aldehyde/ketone (0.10 mmol), aniline (0.10 mmol) and trimethylsilyl cyanide (TMSCN) (0.12 mmol) was combined in a reaction tube. To the mixture, the catalyst (0.01 g) was added. The reaction mixture was stirred for a duration of 5 h. Following the completion of the reaction time, CH_2Cl_2 (0.5 mL) was introduced to each reaction mixture. The MMT-silica-GO-CTU was separated and retrieved through centrifugation at 500 revolutions per minute (rpm). Subsequently, the resulting filtrate underwent evaporation under reduced pressure. It should be noted that the same standard reaction conditions were employed for all the tested substrates in order to facilitate comparison, and therefore, no further optimization of reaction parameters was conducted for individual substrates. [33–35]

6.2.6 Recycling of catalyst

Following the end of the reaction, the MMT-silica-GO-CTU was recovered using the centrifugation technique. Catalyst was then washed with CH_2Cl_2 and subsequently dried under

vacuum for a duration of 3 h. This dried catalyst was then ready for reuse in subsequent catalytic reactions.[36]

6.3 Results and discussion

6.3.1 FTIR spectra

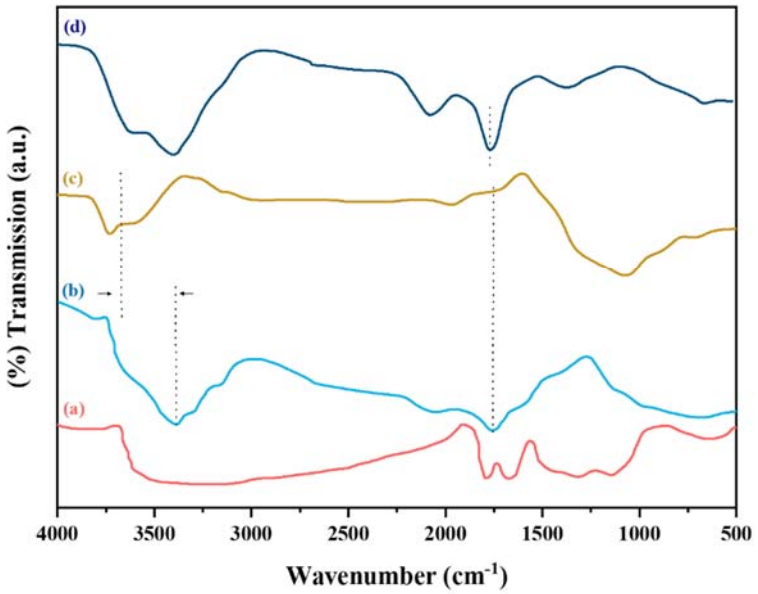

Figure 6.1 FT-IR spectra of (a) GO, (b) MMT, (c) MMT-silica-GO and (d) MMT-silica-GO-CTU.

To confirm the existence of silica and GO on the surface of the MMT in the MMT-silica-GO hybrid composite and MMT-silica-GO-CTU, Fourier transform infrared (FT-IR) spectra were empolyed (*Figure 6.1*). The FT-IR spectrum of GO (*Figure 6.1*(a)) exhibits peaks at 3446 cm^{-1} and 1391 cm^{-1}, corresponding to the deformation of the −OH bond and CO−H groups of GO, respectively. The peak at 1064 cm^{-1} indicates the stretching vibration of the C−O bond. The presence of carbonyl or carboxyl groups was demonstrated by a peak at 1726 cm^{-1}. In the MMT material (*Figure 6.1*(b)), the peak at 3649 cm^{-1} and the broad peak centered at 3469 cm^{-1} were assigned to the O-H stretching vibration of the Si-OH groups within the clay structure. The broad peak at 3469 cm^{-1} can also be attributed to the O-H vibration of water molecules present on the silicate surface. The peak at 1632 cm^{-1} can be assigned to the bending O-H bond of water molecules present within the silicate matrix. On the other hand, the broad peak centered at 1028 cm^{-1} can be attributed to the Si-O-Si groups with the tetrahedral sheet structure. After the reaction with TEOS and

GO, characteristic peaks of both GO and silica were observed (*Figure 6.1*(c)), confirming the fabrication of GO sheets and silica on the surface of MMT. The peak at 500-550 cm^{-1} was attributed to Si−O−Si bending vibration. The appearance of a peak at 1147 cm^{-1} indicates the asymmetric stretching of (Si−O−C/Si−O−Si), while the typical carbonyl group peak at 1714 cm^{-1} disappeared, indicating the conversion of carbonyl groups to Si−O−C bands. The FT-IR spectra of MMT-silica-GO-CTU (*Figure 6.1*(d)) displayed peaks at 3348–3568 cm^{-1}, 1697–1763 cm^{-1}, and 1327–1277 cm^{-1}, corresponding to the ν(N–H), ν(C-O), and ν(C=S) vibrations, respectively, of the encapsulated chiral thiourea scaffolds.[28,37]

6.3.2 Raman spectra

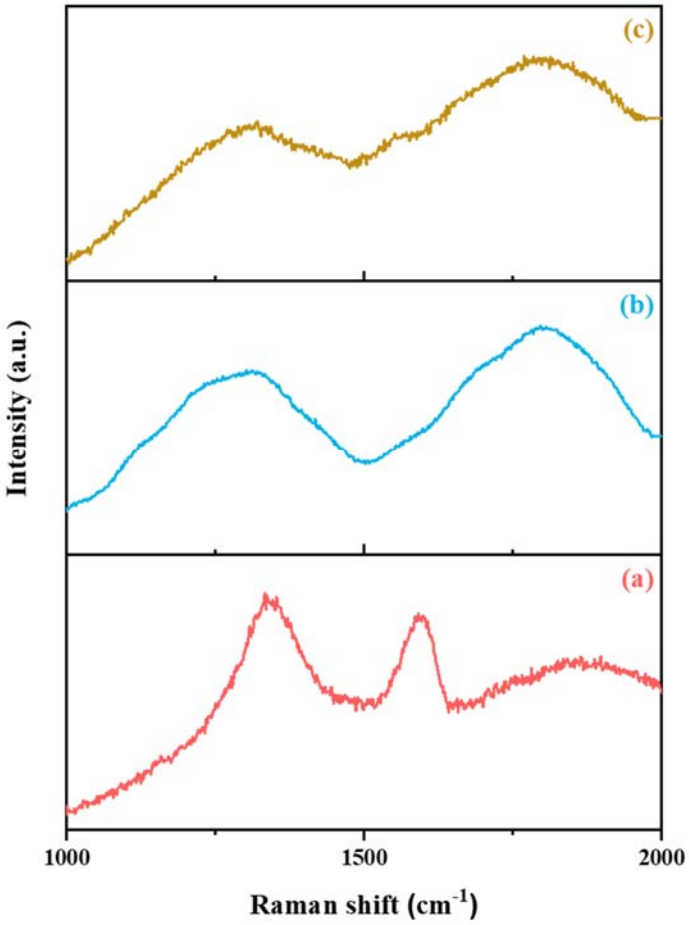

Figure 6.2 Raman spectra of (a) GO, (b) MMT-silica-GO and (c) MMT-silica-GO-CTU.

Raman spectra were utilized to investigate the structural defects of GO, MMT-silica-GO, and MMT-silica-GO-CTU. The Raman bands of GO (*Figure 6.2*(a)), MMT-silica-GO (*Figure 6.2*(b)), and MMT-silica-GO-CTU (*Figure 6.2*(c)) are displayed. All samples exhibits D and G bands as shown in *Figure 6.2*(a). In the MMT-silica-GO composite (*Figure 6.2*(b)), the D and G-bands exhibited a significant reduction in intensity. Additionally, these bands showed significant shifts, indicating a substantial interaction between GO, silica, and MMT. The ID/IG value of the MMT-silica-GO composite was calculated to be 1.32, indicating a modification in the GO structure. MMT-silica-GO-CTU (ID/IG = 1.35) had a higher ID/IG intensity than the GO sheets (1.2), suggesting the presence of disordered carbon increased significantly during composite preparation.[38–43]

6.3.3 BET analysis

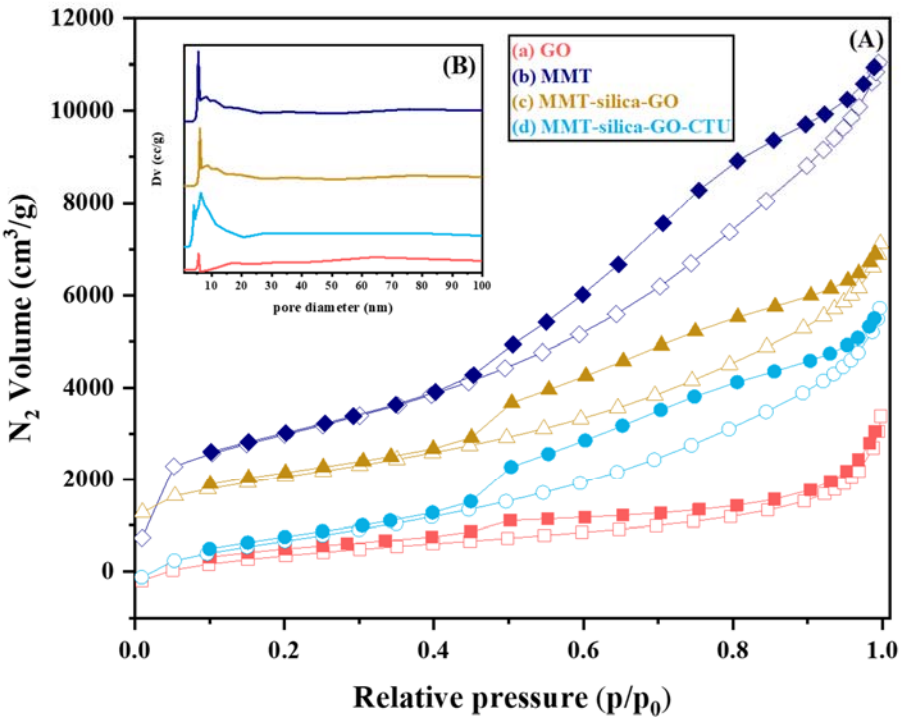

Figure 6.3 N_2 adsorption−desorption isotherms of (a) GO, (b) MMT, (c) MMT-silica-GO and (d) MMT-silica-GO-CTU.

Table 6.1 Textural parameters of catalyst and catalyst precursors.

Sample	Surface area/$m^2\ g^{-1}$	Pore volume/$cm^3\ g^{-1}$	Average pore diameter/nm
GO	105.52	0.11	5.7
MMT	238.14	0.36	6.4
GO-MMT-silica	161.65	0.21	6.1
GO-MMT-silica-CTU	107.31	0.19	5.6

N_2 adsorption-desorption study is a valuable method for determining the surface area and porosity of synthesized compounds. The surface area to volume ratio of the synthesized compounds is an important factor influencing their properties. All the samples revealed similar type IV isotherms, indicating the presence of mesopores, as shown in *Figure 6.3*(A) (a-d). The N_2 adsorption-desorption isotherms and corresponding BJH pore size distributions of GO, MMT, MMT-silica-GO, and MMT-silica-GO-CTU samples are presented in *Figure 6.3*(B) (a-d). The surface area and pore volumes of the four samples are shown in *Table 6.1*. From *Table 6.1*, it can be observed that each material possesses a distinct surface area. Notably, the surface area of the MMT-silica-GO composite significantly decreases after the encapsulation of CTU, indicating the successful encapsulation of the organic scaffold.[44,45]

6.3.4 Scanning electron microscopy

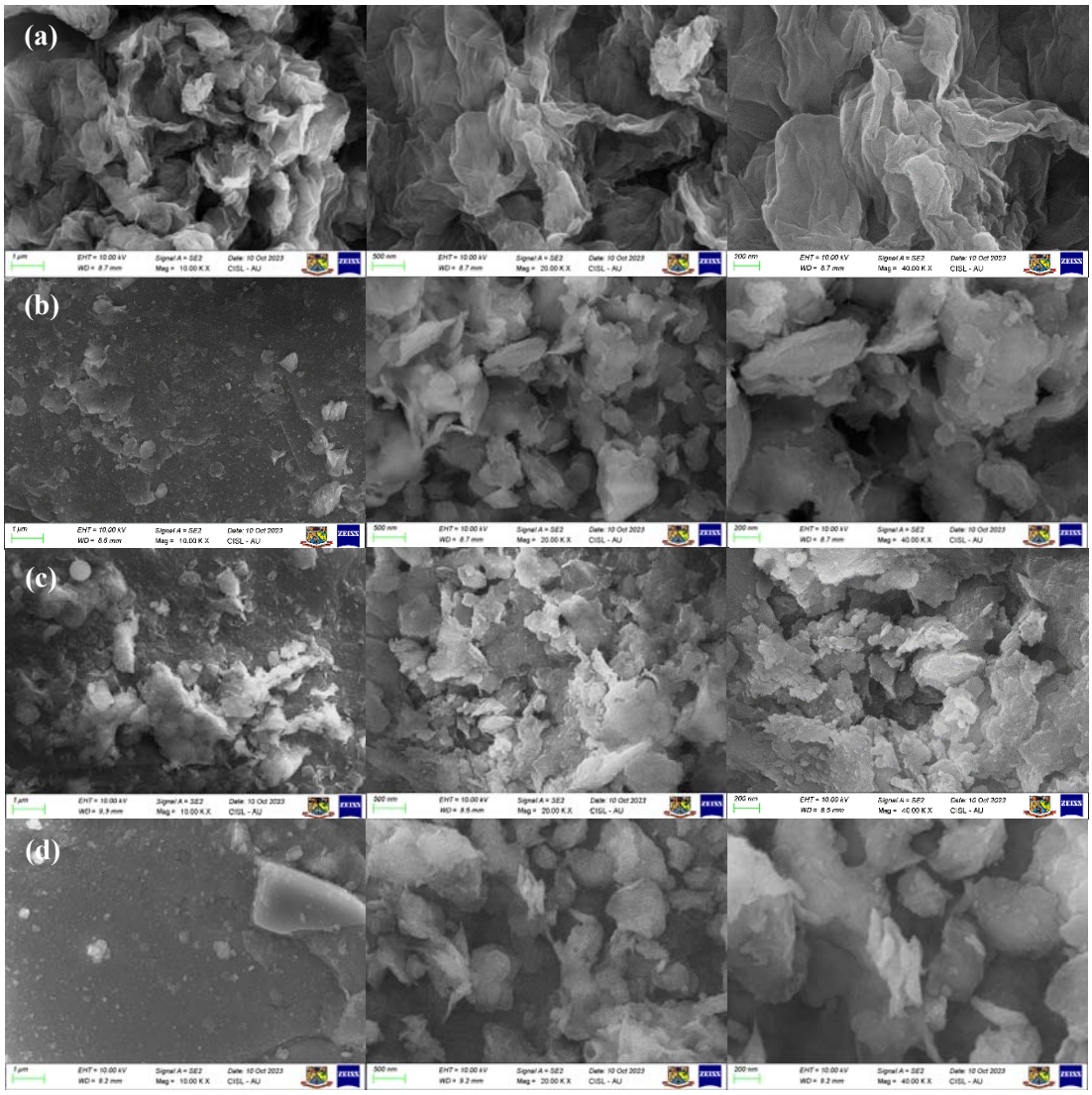

Figure 6.4 FE-SEM images of (a) GO, (b) MMT, (c) MMT-silica-GO and (d) MMT-silica-GO-CTU.

FE-SEM images offer visual confirmation of the folded or wrinkled sheets within the exfoliated GO as depicted in *Figure 6.4*(a). In *Figure 6.4*(b), Montmorillonite presents itself as rock-like macroparticles, characterized by their rugged and densely packed surfaces. Upon the GO modification, *Figure 6.4*(c) reveals the emergence of cracks, resembling long, narrow openings, and the presence of lamellae, which are thin plate-like structures, on the composite's surface. This

observation strongly suggests that the Montmorillonite layer has undergone fractional exfoliation during the GO modification process, likely owing to the intercalation of GO within the Montmorillonite layers. Furthermore, following organic modification, the lamellar edges exhibit a striking brightness, adorned with numerous particles attached to the surface. [28,46]

6.3.5 EDAX spectra

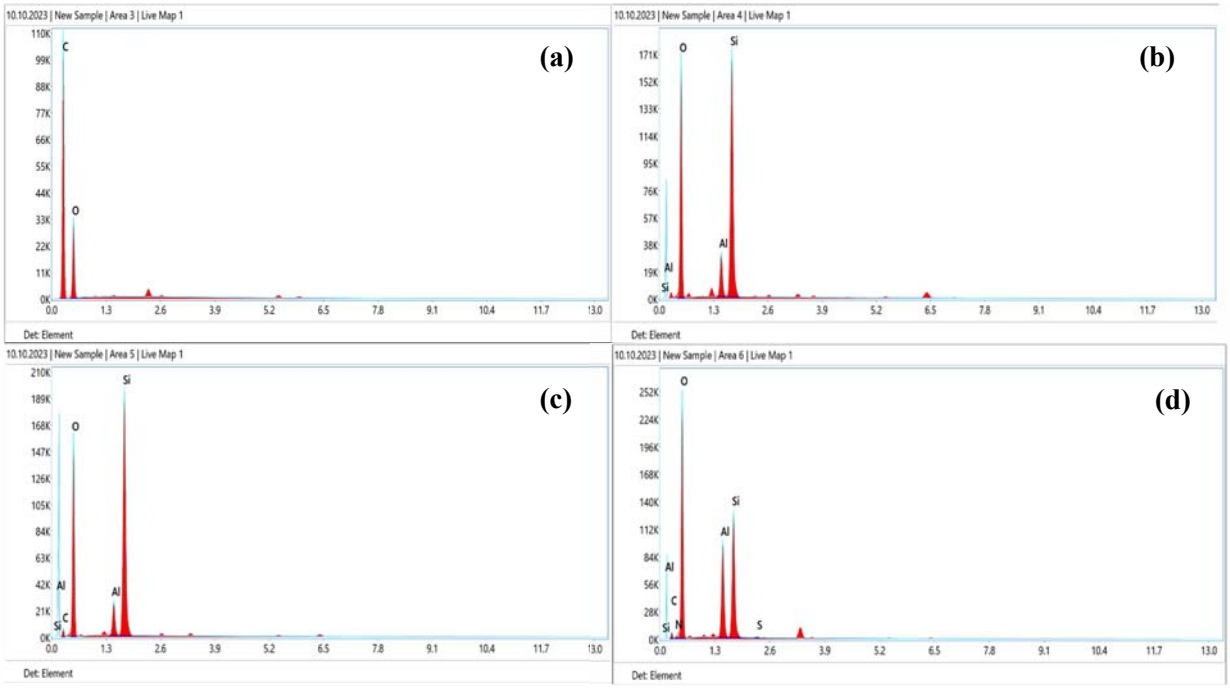

Figure 6.5 EDAX spectra of (a) GO, (b) MMT, (c) MMT-silica-GO and (d) MMT-silica-GO-CTU.

Figure 6.5 illustrates the energy-dispersive X-ray spectra (EDX) of GO, MMT, MMT-silica-GO, and MMT-silica-GO-CTU. As depicted in *Figure 6.5*(a), pure GO primarily consists of carbon (C) 73.09% and oxygen (O) 26.91%. Moving on to *Figure 6.5*(b), MMT is characterized by the presence of silicon (Si) 29.37%, aluminum (Al) 5.47%, and oxygen (O) 65.16%. In *Figure 6.5*(c), the EDX analysis of MMT-silica-GO reveals the composition of silicon (Si) 20.52%, aluminum (Al) 3.07%, oxygen (O) 57.92%, and carbon (C) 18.49%. Lastly, in *Figure 6.5*(d), the EDX spectra of MMT-silica-GO-CTU exhibits the elements silicon (Si) 11.63%, aluminum (Al) 8.86%, oxygen (O) 63.61%, carbon (C) 13.0%, nitrogen (N) 2.76%, and a trace amount of sulfur (S) 0.13%.[27]

6.3.6 X-ray Diffraction Patterns

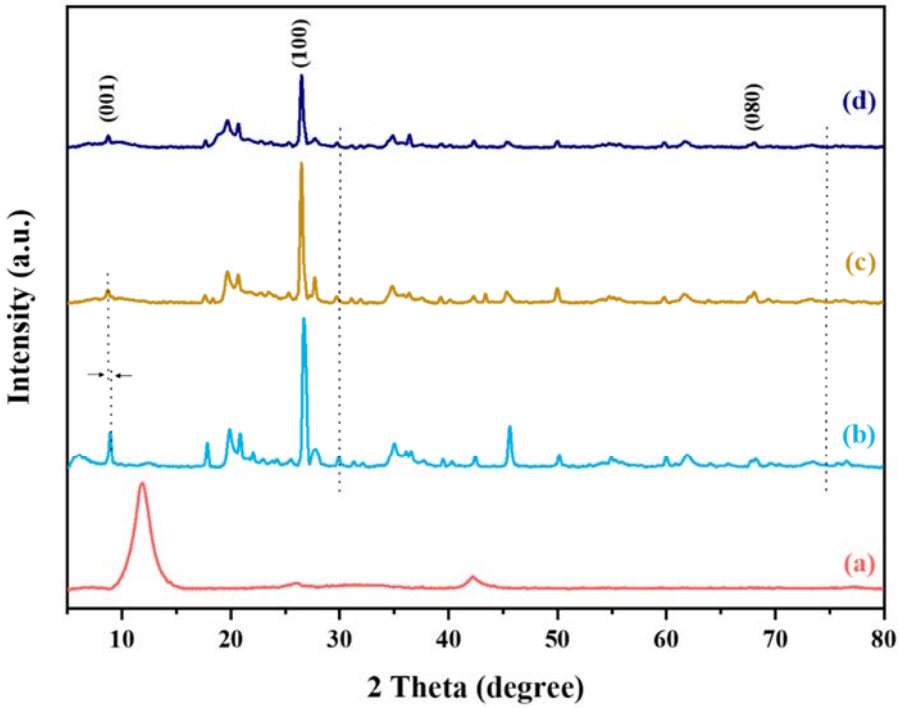

Figure 6.6 XRD patterns of (a) GO, (b) MMT, (c) MMT-silica-GO and (d) MMT-silica-GO-CTU.

X-ray diffraction (XRD) analysis is a reliable technique for assessing the exfoliation degree of MMT in silica and graphene oxide-based composite. The XRD patterns of GO, MMT, MMT-silica-GO composite, and MMT-silica-GO-CTU are displayed in *Figure 6.6* (a-d), respectively. The prominent peaks for MMT are observed at approximately 2θ values of 19.8°, 22.0°, 35.0°, and 61.9°. The XRD curves of MMT, MMT-silica-GO, and MMT-silica-GO-CTU, all exhibit a prominent peak at 2θ = 26.7°, corresponding to the quartz phase, signifying the presence of quartz in the MMT.[44] The presence of the (080) reflection at 2θ = 68.1° also indicates a dioctahedral structure for MMT. Additionally, the peaks attributed to the MMT filler at 2θ > 35° was disappeared. Besides this, the variance between the 2θ values of each peak in the patterns is within a range of 0.5°. The introduction of different GO and silica matrices alters the intensity and width of the peak, which may be attributed to the alignment of MMT sheets between silica and GO, leading to steric hindrances and increased distance between GO sheets, causing structural disruption. These observations provide evidence of proper nanofiller distribution within the GO

and silica matrix. The XRD patterns of the MMT-silica-GO and MMT-silica-GO-CTU composites reveal a less intense and broad amorphous peak at 2θ = 20.8°. This peak could potentially originate from the partially ordered structure of the hard and soft segments present in the silica matrix. The XRD patterns also enable the evaluation of the basal spacing between clay layers, with a diffraction peak of the (001) plane observed at 2θ = 8.9°. After adsorbing GO and silica onto the MMT-silica-GO composite, the *d*-spacing (001) values increase, indicating intercalation of GO and silica molecules into the interlayer of the MMT.[47] During the fabrication processes, the (001) reflection of MMT gradually shifts from 8.9° to 8.6°, signifying the construction of an exfoliated structure resulting from the addition of GO. These findings suggest the successful synthesis of the MMT-silica-GO composite with an exfoliated structure facilitated by GO addition.[48]

6.3.7 SAXS patterns

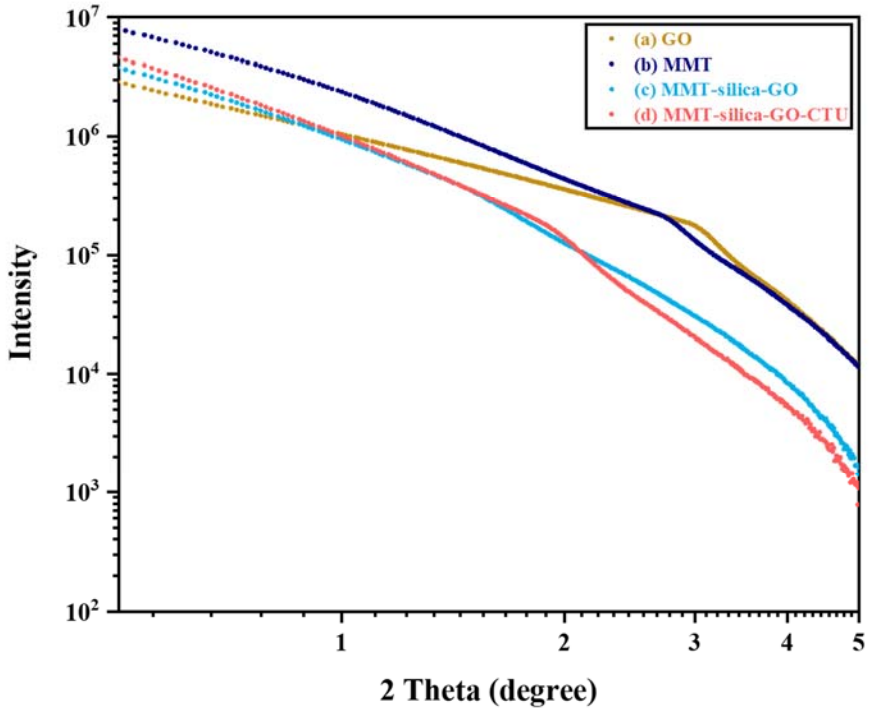

Figure 6.7 SAXS patterns of (a) GO, (b) MMT, (c) MMT-silica-GO and (d) MMT-silica-GO-CTU.

Small-angle X-ray scattering (SAXS) was applied to examine the alterations in structural morphology within the composites, comparing to the neat MMT. It was determined whether MMT and GO were exfoliated by identifying a peak at a very low angle. The experimental SAXS data obtained from the GO and MMT suspension (*Figure 6.7*(a, b)) confirmed the anticipated decrease in scattered intensity as a function of 2θ, indicating the presence of flat objects. Notably, no stacking peaks were observed, suggesting that GO was dispersed entirely as individual sheets (*Figure 6.7*(c)). The scattering profiles of the MMT-silica-GO composite revealed a reciprocal relationship between the lower 2θ scattering and the *d*-spacing. These findings suggest the achievement of an exfoliated structure in the composite. Consequently, the addition of GO and silica led to a redistribution of the MMT within the composite. Notably, a decrease in the characteristic low 2θ exponent was observed in the MMT-silica-GO and MMT-silica-GO-CTU (*Figure 6.7*(d)) compared to neat MMT, indicating an enhanced distance between the MMT layers.[49–51]

6.3.8 X-ray photoelectron spectroscopy

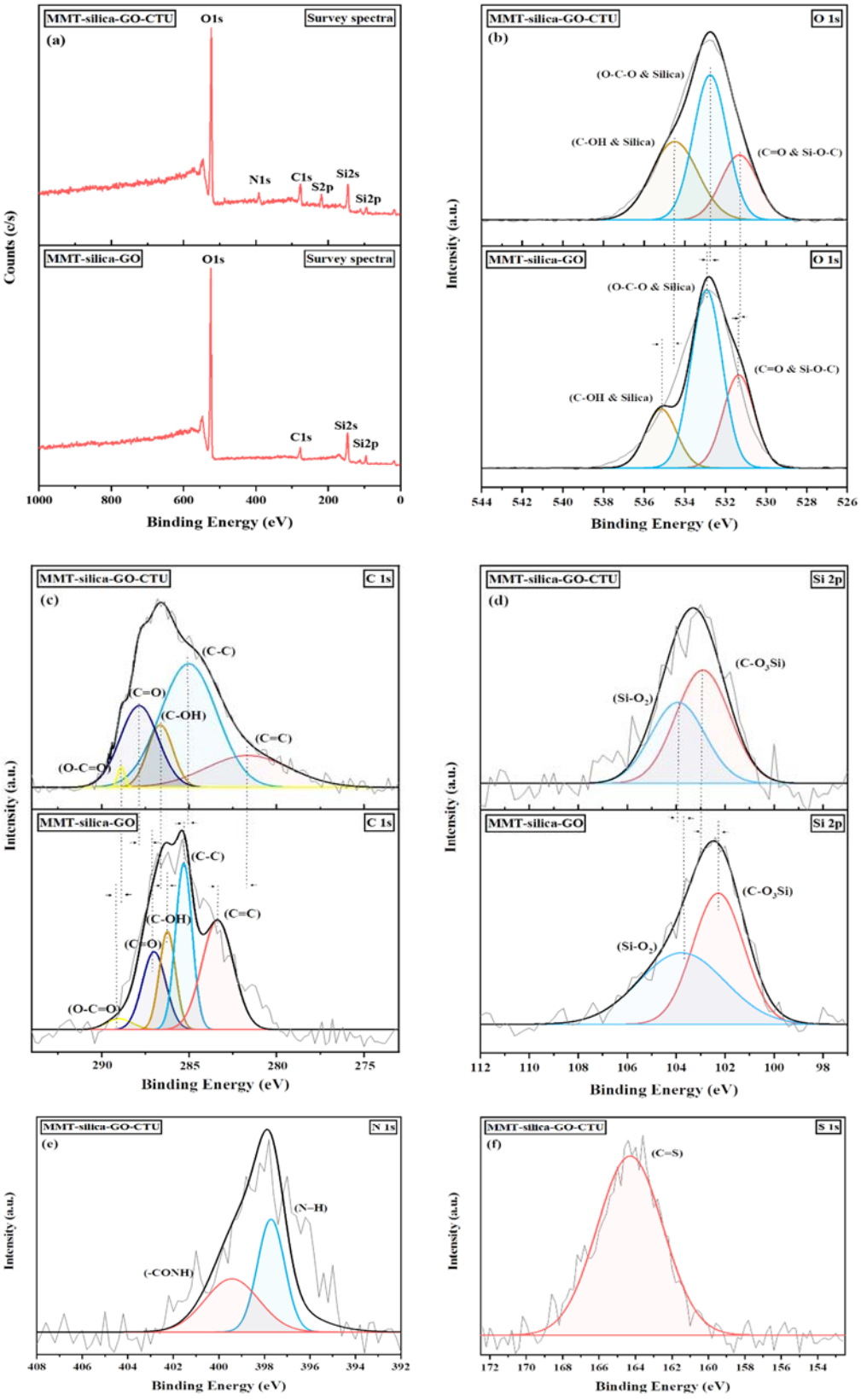

Figure 6.8 (a) Survey XPS spectra of MMT-silica-GO and MMT-silica-GO-CTU (b) O 1s XPS spectra of MMT-silica-GO and MMT-silica-GO-CTU (c) C 1s XPS spectra of MMT-silica-GO and MMT-silica-GO-CTU (d) Si 1s XPS spectra of MMT-silica-GO and MMT-silica-GO-CTU (e) N 1s XPS spectra of MMT-silica-GO-CTU and (f) S 1s XPS spectra of MMT-silica-GO-CTU.

X-ray photoelectron spectroscopy (XPS) was used to examine the surface composition variations of MMT-silica-GO and MMT-silica-GO-CTU. *Figure 6.8*(a) displays the elements observed in the XPS survey spectra of the composite and the composite with encapsulated organic (CTU) scaffold. The O 1s spectra curve fitting (*Figure 6.8*(b)) for MMT-silica-GO revealed peaks at approximately 531.3; 532.9; and 535 eV, corresponding to C=O and Si-O-C; O-C-O and silica; as well as C-OH and silica moieties, respectively. Similarly, for MMT-silica-GO-CTU, the peaks at approximately 531.2; 532.7; and 534.4 eV were assigned to C=O and Si-O-C; O-C-O and silica, as well as C-OH and silica moieties, respectively, with a slight change in binding energy. The C 1s photoelectron peak of MMT-silica-GO (*Figure 6.8*(c)) was analyzed, revealing five distinct symmetrical peaks observed at 284.5, 285, 286.1, 287.2, and 289.1 eV. These peaks correspond to different carbon environments, including nonfunctionalized carbon sp^2 and sp^3 atoms, as well as carbon atoms bonded to oxygen atoms in the form of C-O-, C=O, and COO- groups. The peaks for MMT-silica-GO-CTU were observed at 283.1, 284.9, 285.9, 287.1, and 288.9 eV, again with a slight change in binding energy. The curve fitting of the Si 2p spectra (*Figure 6.8*(d)) showed peak at approximately 103.6 eV, indicating the formation of a silica network, and peak at 102.3 eV, indicating covalent bonding between MMT, GO, and silica. Similarly, for MMT-silica-GO-CTU, the peaks were observed at 103.9 and 102.8 eV, with a slight change in binding energy. The shift values of O 1s, C 1s, and Si 2p binding energies indicated the hybridization of the active groups of CTU with the surface groups of MMT-silica-GO. Furthermore, the N 1s spectra of MMT-silica-GO-CTU (*Figure 6.8*(e)) showed two intense peaks at 397.7 eV (-CONH) and 399.4 eV (N-H), while the S 1s spectra (*Figure 6.8*(f)) displayed a peak at 164.2 eV, possibly due to photoemission from the C=S group.[28,44,46,52–55]

6.3.9 Thermogravimetric study

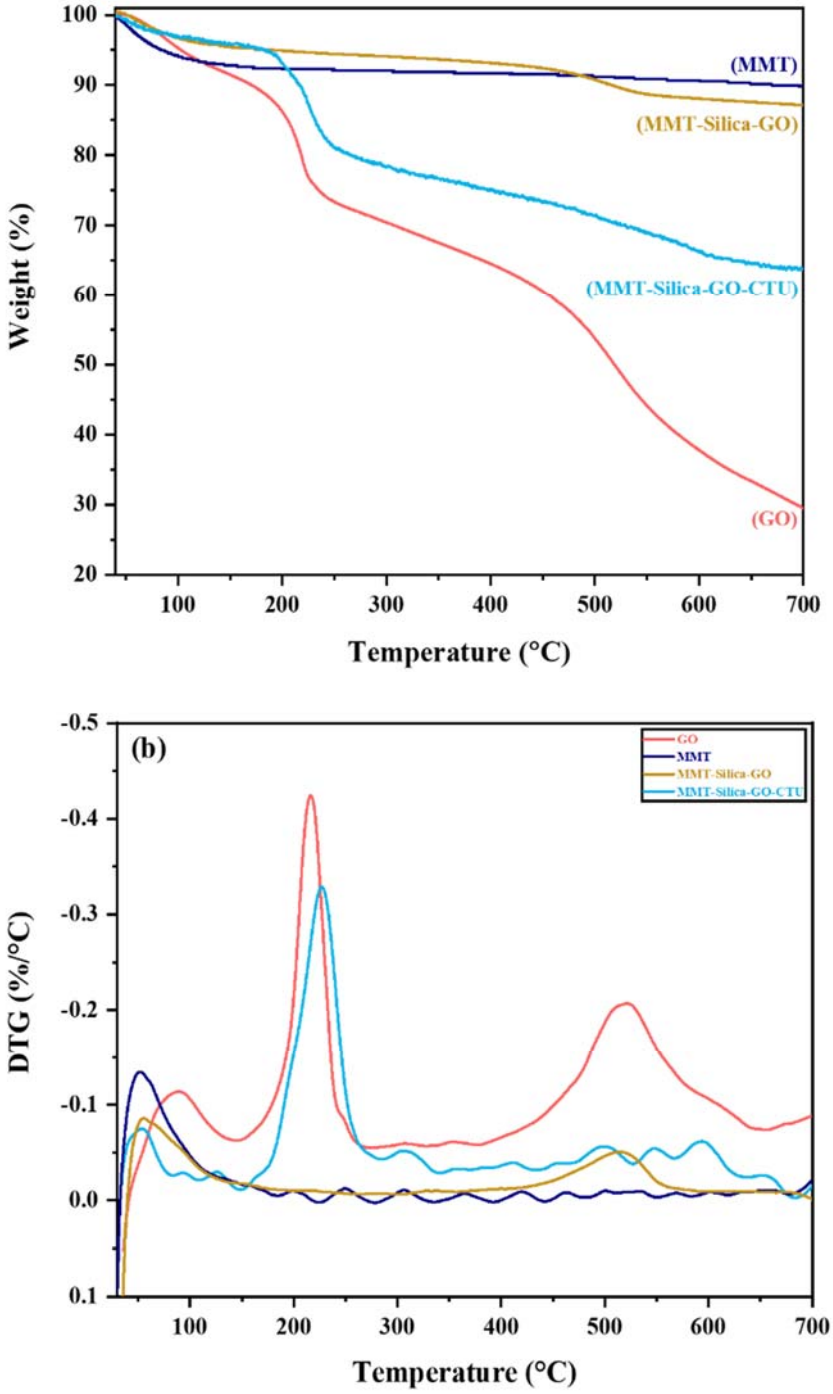

Figure 6.9 (a) TGA curves of GO, MMT, MMT-silica-GO and MMT-silica-GO-CTU, (b) DTG curves of GO, MMT, MMT-silica-GO and MMT-silica-GO-CTU.

In order to determine the thermal stability of synthesized materials, TGA analysis is conducted as provided in *Figure 6.9*(a). In the case of GO, the initial weight loss observed up to 150°C is typically attributed to the evaporation and removal of adsorbed water molecules. However, significant weight loss occurs at approximately 285 °C due to the decomposition of labile oxygen-containing functional groups. For MMT, the initial weight loss up to 150 °C is associated with the collapse of the clay layers and the loss of catalytic activity sites. In contrast, the MMT-silica-GO composite exhibits improved thermal stability compared to MMT and GO. The presence of a GO and silica layers on the surface prevents further degradation. The weight loss of the MMT-silica-GO composite is significantly lower at 400 °C, and the weight remains relatively constant above 350 °C. This excellent thermal stability, combined with the unique sandwich structure of the composite, makes it an ideal reinforcement material for enhancing the thermal stability and catalytic activity of MMT. Regarding the MMT-silica-GO-CTU composite, the TGA analysis reveals three-steps decomposition process. The first step involves the loss of lattice water molecules in the temperature range of 50 to 180 °C, resulting in a mass loss of 5.37%. The second step occurs between 180 and 270 °C with a mass loss of 14.86%, likely corresponding to the decomposition of carboxyl groups. The third step, observed in the temperature range of 270–600 °C, involves the breakdown of the amine and thio-based organic scaffolds, leading to a weight loss of 13.75%.[46,54,56]

The derivative (DTG) curves are depicted in *Figure 6.9*(b). It is evident that all samples exhibit a prominent shoulder peak followed by a sharp decomposition peak. The shoulder peak is indicative of the initial weight loss, occurring within the temperature range of 75°C to 150°C. This weight reduction can be attributed to the degradation of adsorbed water molecules. GO and MMT-silica-GO-CTU shows the mass loss between 180 and 270 °C, likely corresponding to the decomposition of carboxyl groups and organic moiety. On the DTG curve, the sharp peak represents a subsequent weight loss, taking place between 450°C and 550°C, primarily arising from the degradation of the primary carbonaceous compounds. Notably, for the MMT-silica-GO samples, these temperature ranges 75°C and 150°C peak height is decreased, indicating an enhancement in thermal stability. This phenomenon can be attributed to the improved sandwich structure resulting from the uniform dispersion of silica and graphene oxide within MMT. Conversely, a continuous MMT-silica-GO network forms through the even dispersion of silica and

graphene oxide, consequently reducing the rate of volatilization during the initial MMT decomposition. In summary, the incorporation of silica and GO leads to higher heat capacity in composites and enhances the catalytic effect of MMT-silica-GO, resulting in improved thermal stability stemming from increased catalytic activity.[57–59]

Based on the observed results from (FTIR, and Raman) spectra, XRD, SAXS, XPS, and TGA provide conclusive evidence of the successful synthesis of MMT-silica-GO and MMT-silica-GO-CTU composites, revealing their structural and thermal properties.

6.4 Catalytic activity

The catalytic activity of the MMT-silica-GO-CTU composite was investigated in the one-pot Strecker reaction with aldehydes/ketones. In addition to its structural characteristics, the composite exhibits feature that can enhance its catalytic properties. The chiral thiourea metal-free catalyst and thiourea-based moiety present in MMT-silica-GO-CTU contribute Lewis acid/base bifunctional catalytic sites, making it a promising dual catalyst. The study involved testing the catalytic activity of MMT-silica-GO-CTU in the one-pot Strecker reaction using a screening of catalyst loadings. The reaction was then scaled up, and leaching was evaluated. The reaction mixture consists of varying aldehydes/ketones, aniline, and TMSCN in a ratio of 1:1:1.2. By conducting these experiments, the researchers aimed to assess the efficiency and effectiveness of MMT-silica-GO-CTU as a catalyst in promoting the Strecker reaction (*Scheme 6.2* & *Scheme 6.3*). The results would provide insights into its potential as a catalytic system for synthesizing amino nitriles through a convenient and sustainable one-pot process.

6.4.1 Using different types of aldehyde and amines derivatives

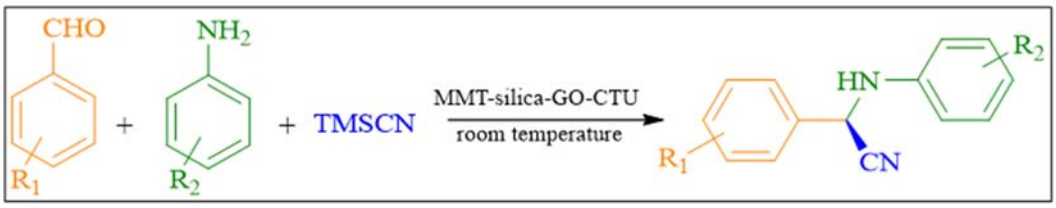

Scheme 6.2 Strecker reaction of various aldehydes and amines in the presence of MMT-silica-GO-CTU.

Table 6.2 Different types of aldehyde and amine derivatives, % conversion and excess of enantiomer (ee) catalyzed by MMT-silica-GO-CTU in the asymmetric Strecker reaction.

Entry	Substrates (R_1 and R_2)	Conversion (%) [a]	ee (%) [b]
1	R_1= H, R_2= H	95	94.61
2	R_1= 4-NO_2, R_2= H	97	96.68
3	R_1=4-Cl, R_2= H	91	96.87
4	R_1=4-Me, R_2= H	91	96.46
5	R_1=4-OH, R_2= H	88	95.24
6	R_1= 4-OMe, R_2= H	87	90.19
7	R_1= 2-OH, R_2= H	84	95.00
8	R_1= H, R_2= 4-NO_2	90	90.00
9	R_1= H, R_2= 2-NO_2,4-Cl	87	87.56
10	R_1= H, R_2= 4-OH	86	86.69
11	R_1= H, R_2= 4-OMe	85	86.22
12	R_1= H, R_2= 2-OH	83	82.54

Reaction condition: aldehyde (0.10 mmol), amines (0.10 mmol) and trimethylsilyl cyanide (TMSCN) (0.12 mmol), catalyst (MMT-silica-GO-CTU) (0.01 g), The reaction mixture was stirred for 5 h at room temperature. [a]Isolated yields. [b]Identified through chiral HPLC analysis.

6.4.2 Testing MMT-silica-GO-CTU recyclability with aldehyde and amine

Table 6.3 Recyclability test of the MMT-silica-GO-CTU over the asymmetric strecker reaction.

Entry	Conversion (%) [a]	ee (%) [b]
1	95	94.61
2	93	92.71
3	89	91.00
4	87	87.52
5	84	86.61

Reaction condition: benzaldehyde (0.10 mmol), aniline (0.10 mmol) and trimethylsilyl cyanide (TMSCN) (0.12 mmol), catalyst (MMT-silica-GO-CTU) (0.01 g), The reaction mixture was stirred for 5 h at room temperature. [a]Isolated yields. [b]Identified through chiral HPLC analysis.

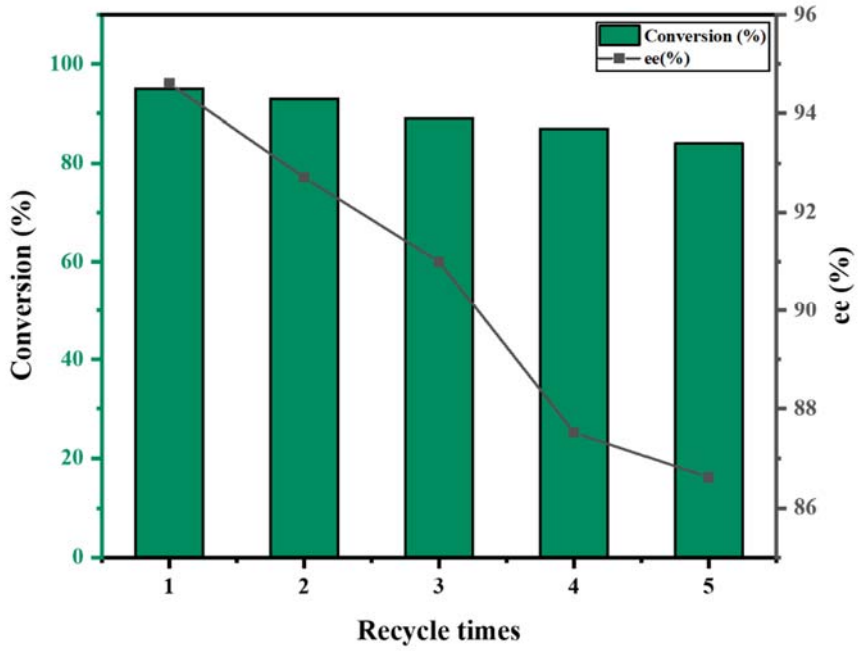

Figure 6.10 Recyclability test of MMT-silica-GO-CTU catalyst over the asymmetric strecker reaction.

6.4.3 Using types of ketones and amines derivatives

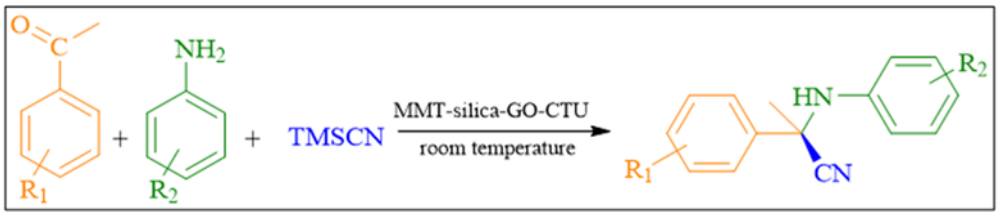

Scheme 6.3 Strecker reaction of various ketones and amines in the presence of MMT-silica-GO-CTU

Table 6.4 Different types of ketone and amine derivatives, % conversion and excess of enantiomer (ee) catalyzed by MMT-silica-GO-CTU in the asymmetric Strecker reaction.

Entry	Substrates (R_1 and R_2)	Conversion (%) [a]	ee (%) [b]
1	R_1= H, R_2= H	90	91.01
2	R_1=4-Cl, R_2= H	83	92.75
3	R_1=4-OH, R_2= H	83	84.55
4	R_1=4-NH_2, R_2= H	79	81.09
5	R_1=H, R_2= 4-NO_2	80	80.55
6	R_1= H, R_2= 2-NO_2,4-Cl	78	79.16
7	R_1= H, R_2= 4-OH	76	77.20
8	R_1= H, R_2= 2-OH	73	74.87
9	R_1= H, R_2= 4-OMe	72	76.10

Reaction condition: ketone (0.10 mmol), aniline (0.10 mmol) and trimethylsilyl cyanide (TMSCN) (0.12 mmol), catalyst (MMT-silica-GO-CTU) (0.01 g), The reaction mixture was stirred for 5 h at room temperature. [a]Isolated yields. [b]Identified through chiral HPLC analysis.

6.4.4 Testing MMT-silica-GO-CTU recyclability with ketone and amine

Table 6.5 Recyclability test of the MMT-silica-GO-CTU over the asymmetric strecker reaction.

Entry	Conversion (%) [a]	ee (%) [b]
1	90	91.01
2	89	90.15
3	85	87.56
4	83	86.22
5	81	84.51

Reaction condition: acetophenone (0.10 mmol), aniline (0.10 mmol) and trimethylsilyl cyanide (TMSCN) (0.12 mmol), catalyst (MMT-silica-GO-CTU) (0.01 g), The reaction mixture was stirred for 5 h at room temperature. [a]Isolated yields. [b]Identified through chiral HPLC analysis.

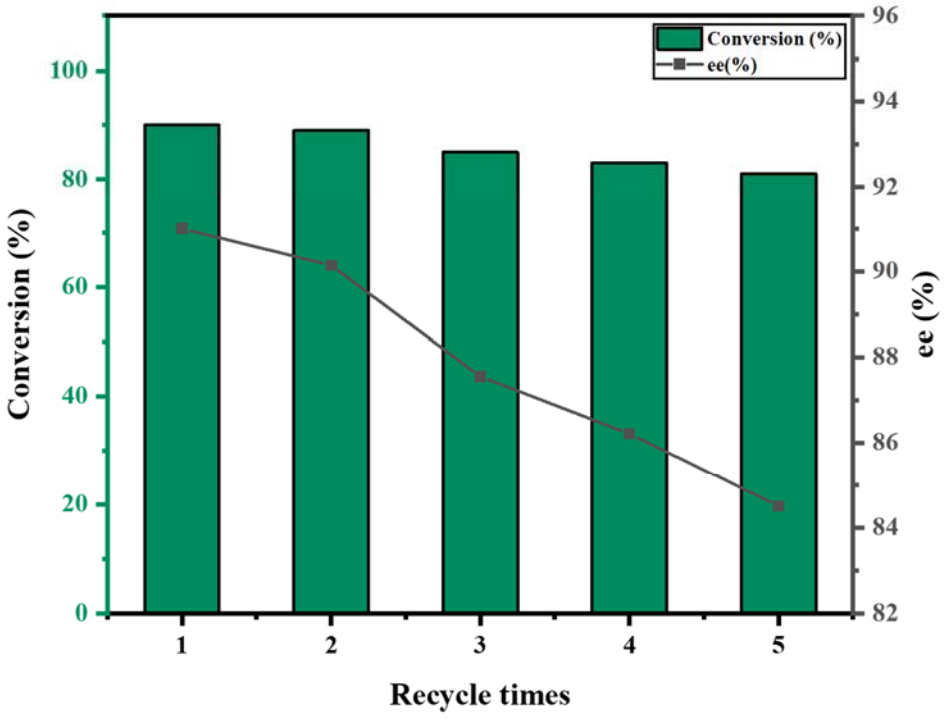

Figure 6.11 Recyclability test of MMT-silica-GO-CTU catalyst over the asymmetric strecker reaction.

In this study, the asymmetric cyanosilylation of benzaldehyde (for various aldehydes) and acetophenone (for various ketones) was selected as a representative reaction to synthesize chiral cyanohydrins under mild reaction conditions. In this study, MMT-silica-GO-CTU was used as the catalyst, and various solvents were tested to determine the optimal solvent for the highest product yield and enantioselectivity. Notably, the absence of the catalyst led to a complete lack of enantioselectivity, resulting in a zero percent enantiomeric excess (ee). This finding suggests that the chiral nature of the product was solely derived from the intrinsic chirality of the MMT-silica-GO-CTU catalyst. Different aldehydes and ketones were tested under optimized reaction conditions using MMT-silica-GO-CTU as a catalyst. The results were summarized in *Table 6.2 & Table 6.4*. The study also investigated the influence of substituent groups on the electronic effects and steric hindrance of the aldehydes/ketones. It was observed that electron-withdrawing and electron-donating substituents led to the formation of cyanohydrins with good-to-excellent yields. The enantioselectivity of the synthesized products was observed to be strongly influenced by the electronic properties and steric hindrance of the substituent groups. These results indicated that MMT-silica-GO-CTU acted as an asymmetric heterogeneous catalyst. The stability of MMT-silica-GO-CTU after catalytic run was evaluated. The catalyst could be readily separated from the reaction suspension using a simple centrifugation process and demonstrated the ability to be reused for at least five cycles. Throughout the recycling process, there was only a slight reduction in both reactivity and enantioselectivity of the catalyst. The results are summarized in *Table 6.3* & *Table 6.5* and are depicted in *Figure 6.10* & *Figure 6.11*. Analysis of the catalyst's stability was performed using various techniques including PXRD, FTIR, Raman spectroscopy SEM and EDAX (*Figure 6.12* (a-e)).

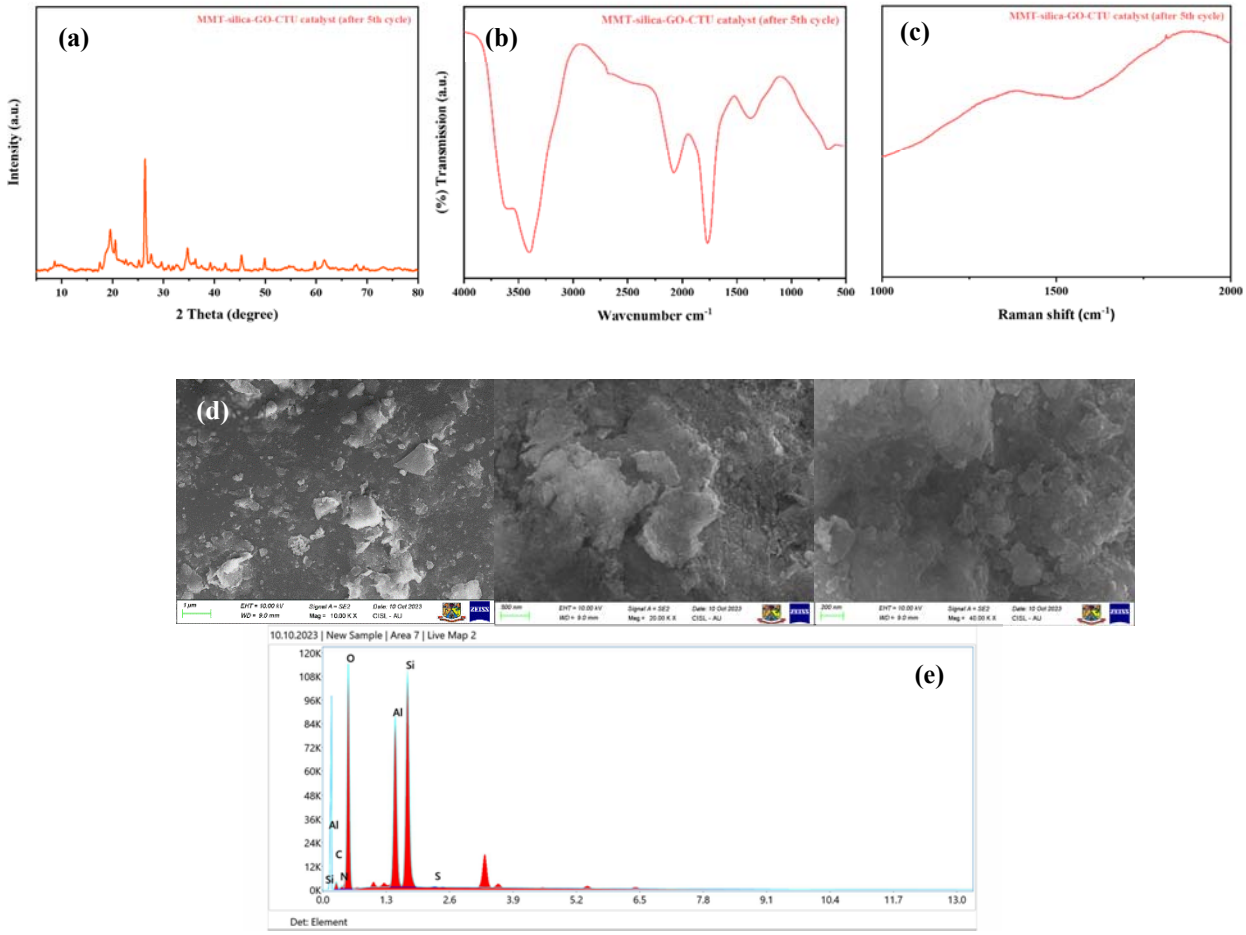

Figure 6.12 (a) XRD pattern of the MMT-silica-GO-CTU catalyst (after 5th cycle), (b) Raman spectra of the MMT-silica-GO-CTU catalyst (after 5th cycle). (c) FTIR spectra of the MMT-silica-GO-CTU catalyst (after 5th cycle). (d) FESEM image of the MMT-silica-GO-CTU catalyst (after 5th cycle). (e) EDAX spectra of the MMT-silica-GO-CTU catalyst (after 5th cycle).

The PXRD patterns, crystallinity, FTIR and Raman spectra of MMT-silica-GO-CTU remained unchanged after 5th cycle, indicating the stability of the catalyst was intact throughout the reaction cycles. These findings demonstrate the effectiveness and stability of MMT-silica-GO-CTU as an asymmetric heterogeneous catalyst for the cyanosilylation reaction, offering potential applications in the synthesis of chiral cyanohydrins.

6.5 A plausible catalytic path for asymmetric Strecker reaction

Based on the above studies, a proposed mechanism for the Strecker reaction catalyzed by MMT-silica-GO-CTU is illustrated in the accompanying *Figure 6.13*. The findings and proposed mechanism presented in this work are consistent with the reports found in the literature.[15,33,60] Previous studies have indicated that the reaction involves the interaction between the oxygen of aldehydes/ketones and the Lewis acidic site (amine group) present in MMT-silica-GO-CTU. The interaction between the oxygen of aldehydes/ketones and the Lewis acidic site (amine group) in MMT-silica-GO-CTU enhances the carbonyl carbon electrophilicity. This increased electrophilicity promotes the nucleophilic attack of the amine on the carbonyl carbon of benzaldehyde, leading to the generation of an imine intermediate. Subsequently, a water molecule is eliminated from the intermediate, resulting in the formation of the desired product. Furthermore, the imine nitrogen undergoes polarization due to the presence of the amine group. This mutual polarization additionally amplifies the electrophilic nature of the imine intermediate, which is generally characterized as a weak electrophile. This increased electrophilicity enables, the nucleophilic attack by the CN- group of TMSCN undergoes a nucleophilic attack, leading to the formation of α-aminonitriles. Additionally, this process leads to the regeneration of the active form of the catalyst, thus completing the catalytic cycle.

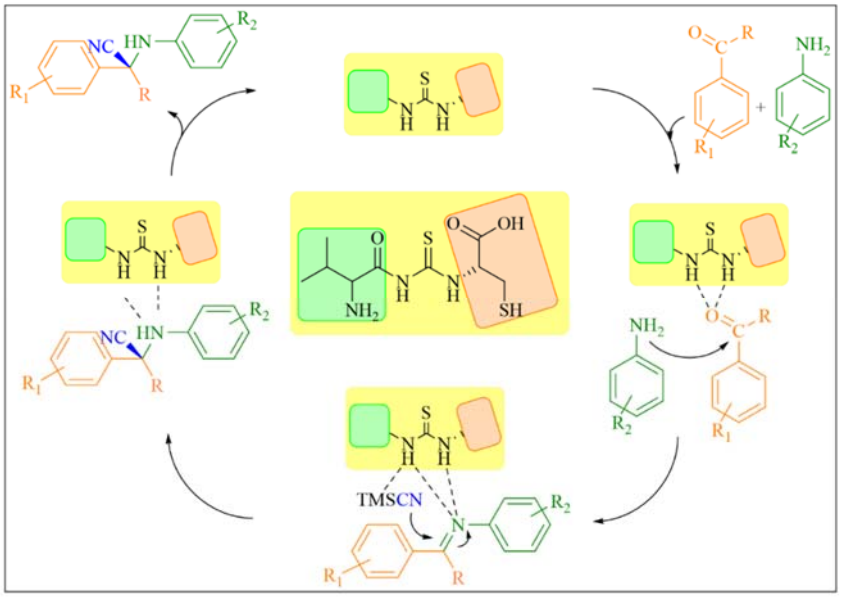

Figure 6.13 A plausible catalytic cycle for asymmetric Strecker reaction.

6.6 Conclusion

In conclusion, the research presented here focuses on the synthesis and characterization of composites comprising montmorillonite, silica, and graphene oxide (MMT-silica-GO). The successful intercalation of graphene oxide sheets and silica into the MMT interlayer. One notable finding is that the MMT-silica-GO composite exhibits improved thermal stability when compared to individual components, namely MMT and GO. This enhanced thermal stability is a significant advantage and expands the potential applications of these composites, which enhances the accessibility of active sites and promotes efficient dispersion of the catalyst. These findings highlight the importance of composite materials and their potential for applications in catalysis. Furthermore, the developed a novel variation of the composite material, MMT-silica-GO, by encapsulating it with a chiral thiourea-based moiety (CTU). The catalytic performance of the MMT-silica-GO-CTU composite was evaluated for the Strecker reaction. The results demonstrate that this composite material exhibits high catalytic activity and selectivity in the Strecker reaction, suggesting its potential as an efficient catalyst.

6.7 References

1. Zhou, C. H. An overview on strategies towards clay-based designer catalysts for green and sustainable catalysis. *Appl. Clay Sci.* **2011**, 53, 87–96.
2. Lakhani P., Chodvadiya D., Jha P. K., Gupta V., Trzybiński D., Wozniak K., Kurzydłowski K., Goutam U. K., Srivastava H. and Modi C. K., DFT stimulation and experimental insights of chiral Cu(II)-salen scaffold within the pocket of MWW-zeolite and its catalytic study. *Phys. Chem. Chem. Phys.*, **2023**, 25, 14374-14386.
3. Kundu, S., Manor, N. K. and Radian, A. Iron-Montmorillonite-Cyclodextrin Composites as Recyclable Sorbent Catalysts for the Adsorption and Surface Oxidation of Organic Pollutants. *ACS Appl. Mater. Interfaces* **2020**, 12(47), 52873–52887.
4. Lakhani, P. & Modi, C. K. Shaping enantiochemistry : Recent advances in enantioselective reactions via heterogeneous chiral catalysis. *Mol. Catal.* **548**, 113429 (2023).
5. Jha, A., Garade, A. C., Shirai, M. and Rode, C. V. Metal cation-exchanged montmorillonite clay as catalysts for hydroxyalkylation reaction. *Appl. Clay Sci.* **2013**, 74, 141–146.

6. Kumar B.S., Dhakshinamoorthy A., and Pitchumani K., K10 montmorillonite clays as environmentally benign catalysts for organic reactions. *Catal. Sci. Technol.* **2014**, 4(8), 2378–2396.
7. Sultana, S., Borah, G. and Gogoi, P. K. Mont-K10 Supported Fe (II) Schiff-Base Complex as an Efficient Catalyst for Hydrogenation of Ketones. *Catal. Letters,* **2019**, 149, 2142–2157.
8. Heydari A. and Sheibani H., Fabrication of poly(β-cyclodextrin-co-citric acid)/bentonite clay nanocomposite hydrogel: thermal and absorption properties. *RSC Adv.* **2015**, 5(100), 82438–82449.
9. Lakhani, P. and Modi, C. K.. Asymmetric Hydrogenation using Covalently Immobilized Ru-BINOL-AP@MSNs Catalyst. *New J. Chem.* **2023,** 47, 8767–8775.
10. Lakhani, P. and Modi, C. K. Spick-and-span protocol for designing of silica-supported enantioselective organocatalyst for the asymmetric aldol reaction. *Mol. Catal.*, **2022,** 525, 112359.
11. Lakhani, P., Kane, S., Srivastava, H., Goutam, U. K. & Modi, C. K. *RSC Sustain.*, **2023**, 1, 1773-1782.
12. Wang Y., Chi B., Xiao C., Chen D., Wang Y., and Liu M., Graphene Oxide@Mg3Si4O9(OH)10 : A Hierarchical Layered Silicate Nanocomposite with Superior Adsorption Capacity for Enriching Eu (III). *Chem. Eng. J.* **2017**, 338, 628–635.
13. Qu, Y. A. W. and Lu, P. Y. J. The assembly of a composite based on nano-sheet graphene oxide and montmorillonite. *Pet. Sci.,* **2018**, 15, 366–374.
14. Sicignano M., Rodríguez R. I., Capaccio V., Borello F., Cano R., De Riccardis F., Bernardi L., Díaz-Tendero S., Della Sala G., and Alemán J., Asymmetric trifluoromethylthiolation of azlactones under chiral phase transfer catalysis. *Org. Biomol. Chem.*, **2020**, 18(15), 2914–2920.
15. Weng Z. Z., Xie J., Huang K. X., Li J. P., Long L. S., Kong X. J., and Zheng L. S., Asymmetric Cyanosilylation of Aldehydes by a Lewis Acid/Base Synergistic Catalyst of Chiral Metal Clusters. *Inorg. Chem.* **2022**, 61(9), 4121–4129.
16. Blacker J., Clutterbuck L. A., Crampton M. R., Grosjean C. and North M., Catalytic, asymmetric Strecker reactions catalysed by titanium IV and vanadium V (salen) complexes. *Tetrahedron: Asymmetry,* **2006,** 17, 1449–1456.

17. Jarusiewicz J., Choe Y., Yoo K. S., Park C. P., and Jung K. W., Efficient Three-Component Strecker Reaction of Aldehydes/Ketones via NHC-Amidate Palladium (II) Complex Catalysis. *J. Org. Chem.* **2009**, 74, 7, 2873–2876.
18. Tiago G., Mahmudov K., Guedes da Silva M., Ribeiro A., Branco L., Zubkov F., and Pombeiro A., Cyanosilylation of Aldehydes Catalyzed by Ag(I)- and Cu(II)-Arylhydrazone Coordination Polymers in Conventional and in Ionic Liquid Media. *Catalysts,* **2019**, 9(3), 284.
19. Wang, K., Li, H., Yang, L., Liu, Z. and Yao, Z. Half-Sandwich Ruthenium Complexes with Hydrazone Ligands: Preparation, Structure, and Catalytic Activity in Cyanosilylether Synthesis under an Air Atmosphere. *Inorg. Chem.* **2023**, 62(25), 9872–9881.
20. Kouznetsov, V. V and Galvis, C. E. P. Strecker reaction and α-amino nitriles: Recent advances in their chemistry, synthesis, and biological properties. *Tetrahedron* **2018,** 74, 773–810.
21. Hou Y., Sun R. W., Zhou X., Wang J., and Li D., A copper(i)/copper(ii)–salen coordination polymer as a bimetallic catalyst for three-component Strecker reactions and degradation of organic dyes. *Chem. Commun.*, **2014**, 50(18), 2295–2297.
22. Cai X. and Xie B., Recent advances in asymmetric Strecker reactions. *Arkivoc.* **2014**, 2014(1), 205–248.
23. Paulchamy B., Arthi G. and Bd L., A Simple Approach to Stepwise Synthesis of Graphene Oxide. *J. Nanomed. Nanotechnol.*, **2015**, 6, 1000253.
24. Vithalani R., Patel D., Modi C. K., Som N.N., Jha P.K., and Kane S.R., Enhancing the potency of surface hydroxyl groups of graphene oxide for selective oxidation of benzyl alcohol. *Diam. Relat. Mater.* **2018**, 90, 154–165.
25. Patel D., Kane S. R. and Modi C. K. One-pot multistep Henry-Michael reaction with notable upshots using reduced graphene oxide supported bifunctional catalysts. *Catal. Commun.* **2022,** 169, 106476.
26. Ge W., Ma Q., Ai Z., Wang W., Jia F., and Song S., Three-dimensional reduced graphene oxide/ montmorillonite nanosheet aerogels as electrode material for supercapacitor application. *Appl. Clay Sci.,* **2021,** 206, 106022.
27. Dehghani Z., Sedghi-asl M. and Ghaedi M., Ultrasound-assisted adsorption of paraquat herbicide from aqueous solution by graphene oxide/mesoporous silica. *J. Environ. Chem.*

Eng., **2021,** 9, 105043.

28. Zhang W. L. and Choi H. J., Silica-Graphene Oxide Hybrid Composite Particles and Their Electroresponsive Characteristics. *Langmuir* **2012**, 28, 17, 7055–7062.
29. Brito T.O., Souza A.X., Mota Y. C. C., Morais V.S.S., de Souza L.T., de Fátima Â., Macedo F., and Modolo L.V., Design, syntheses and evaluation of benzoylthioureas as urease inhibitors of agricultural interest. *RSC Adv*., **2015,** 5(55), 44507–44515.
30. Abdelgayed W., Arafa A., Ghoneim A. A. and Mourad A. K., N-Naphthoyl Thiourea Derivatives: An Efficient Ultrasonic-Assisted Synthesis, Reaction, and In Vitro Anticancer Evaluations. *ACS Omega,* **2022**, 7(7), 6210–6222.
31. Özgeri B., Design, synthesis, characterization, and biological evaluation of nicotinoyl thioureas as antimicrobial and antioxidant agents. *J Antibiot,* **2021**, 74(4), 233–243.
32. Wu J., Shi Q., Chen Z., He M., Jin L., and Hu D. Synthesis and Bioactivity of Pyrazole Acyl Thiourea Derivatives. *Molecules*, **2012**, 17(5), 5139–5150.
33. Khan S., Markad D., and Mandal S.K., Two Zn(II)/Cd(II) Coordination Polymers as Recyclable Heterogeneous Catalysts for an Efficient Room-Temperature Synthesis of α-Aminonitriles via the Solvent-Free Strecker Reaction. *Inorg. Chem.* **2022**, 62(1), 275–284.
34. Gómez-Oliveira E. P., Méndez N., Iglesias M., Gutiérrez-Puebla E., Aguirre-Díaz L. M., and Monge M. Á. Building a Green, Robust, and Efficient Bi-MOF Heterogeneous Catalyst for the Strecker Reaction of Ketones. *Inorg. Chem.,* **2022**, 61(19), 7523–7529.
35. Belokon Y. N., Green B., Ikonnikov N. S., North M. and Tararov V. I. Optimized catalysts for the asymmetric addition of trimethylsilyl cyanide to aldehydes and ketones. *Tetrahedron* **2001,** 57(4), 771–779.
36. Saravanan S., Khan N. H., Jakhar A., Ansari A., Kureshy R. I., Abdi S. H. R., and Kumar G., Enantioselective Strecker reaction of aldimines using potassium cyanide catalyzed by a recyclable macrocyclic V (V) salen complex. *RSC Adv.* **2015**, 5(121), 99951–99958.
37. Hsiao M.C., Ma C.C.M., Chiang J.C., Ho K.K., Chou T.Y., Xie X., Tsai C.H., Chang L.H., and Hsieh C.K., Thermally conductive and electrically insulating epoxy nanocomposites with thermally reduced graphene oxide–silica hybrid nanosheets. *Nanoscale,* **2013**, 5(13), 5863.
38. Liu L., Guo X., Shi L. and Chen L., SiO2-GO nanofillers enhance the corrosion resistance of waterborne polyurethane acrylic coatings. *Adv. Compos. Lett.* **2020,** 29, 1–9.

39. Medina A., Casado-carmona F. A. and López-lorente Á. I., Magnetic Graphene Oxide Composite for the Microextraction and Determination of Benzophenones in Water Samples. *Nanomaterials*, **2020**, 10(1), 168.
40. Nagashio K., Yamashita T., Fujita, J., Nishimura T., Kita K., and Toriumi A., Impacts of graphene/SiO2 interaction on FET mobility and Raman spectra in mechanically exfoliated graphene films. *IEDM*, **2010**, 564–567.
41. Dong R., Wang L., Zhu J., Liu L. and Qian Y., A novel SiO2–GO/acrylic resin nanocomposite: fabrication, characterization and properties. *Appl. Phys. A.,* **2019,** 125, 1–11.
42. Savchenko D., Vorlíček V., Kalabukhova E., Sitnikov A., Vasin A., Kysil D., Sevostianov S., Tertykh V., and Nazarov A., Infrared , Raman and Magnetic Resonance Spectroscopic Study of SiO 2: C Nanopowders. *Nanoscale Res Lett.,* **2017**, 12(1), 1–12.
43. Miroshnikov Y., Grinbom G., Gershinsky G., Nessim G. D. and Zitoun D., Do we need covalent bonding of Si nanoparticles on graphene oxide for Li-ion batteries?. *Faraday Discuss.* **2014,** 173, 391–402.
44. Xu, W., Chen, Y., Zhang, W. and Li, B., Fabrication of graphene oxide/bentonite composites with excellent adsorption performances for toluidine blue removal from aqueous solution. *Adv. Powder Technol.* **2019**, 30(3), 493–501.
45. Ali B., Yusup S., Quitain A. T., Alnarabiji M. S., Kamil R. N. M., and Kida T., Synthesis of novel graphene oxide/bentonite bi-functional heterogeneous catalyst for one-pot esterification and transesterification reactions. *Energy Convers. Manag.* **2018,** 171, 1801–1812.
46. Wu G., Ma L., Liu L., Chen L. and Huang Y., Preparation of SiO2-GO hybrid nanoparticles and the thermal properties of methylphenylsilicone resins/ SiO2-GO nanocomposites. *Thermochim. Acta,* **2015,** 613, 77–86.
47. Wei J., Aboud M. F. A., Shakir I., Tong Z. and Xu Y. Graphene Oxide-Supported Organo-Montmorillonite Composites for the Removal of Pb (II), Cd (II), and As (V) Contaminants from Water. *ACS Appl. Nano Mater.* **2019**, 3(1), 806-813.
48. Funes I. G. A., Peralta M. E., Pettinari G. R., Carlos L. and Parolo M. E. Facile modification of montmorillonite by intercalation and grafting: The study of the binding mechanisms of a quaternary alkylammonium surfactant. *Appl. Clay Sci.,* **2020,** 195, 105738.

49. Singh V., Varanasi S., Batchelor W. and Garnier G., Materials & Design Cellulose nanocrystals to modulate the self-assembly of graphene oxide in suspension. *Mater. Des.,* **2022,** 216, 110572.
50. Chronopoulou L., Di Nitto A., Papi M., Parolini O., Falconi M., Teti G., Muttini A., Lattanzi W., Palmieri V., Ciasca G., Del Giudice A., Galantini L., Zanoni R., and Palocci C. Colloids and Surfaces B: Biointerfaces Biosynthesis and physico-chemical characterization of high performing peptide hydrogels@graphene oxide composites. *Colloids Surf. B,* **2021,** 207, 111989.
51. Zhu Y., Kottarath S., Iroh J.O., and Vaia R.A., Progressive Intercalation and Exfoliation of Clay in Polyaniline–Montmorillonite Clay Nanocomposites and Implication to Nanocomposite Impedance. *Energies*, **2022**, 15(15), 5366.
52. Narayanan D. P., Gopalakrishnan A., Yaakob Z., Sugunan S. and Narayanan B. N., A facile synthesis of clay-graphene oxide nanocomposite catalysts for solvent free multicomponent Biginelli reaction. *Arab. J. Chem.,* **2017,** 13(1), 318–334.
53. Alexander M. R., Short R. D., Jones F. R., Michaeli W. and Blomfield C.J., A study of HMDSO/O2 plasma deposits using a high-sensitivity and energy resolution XPS instrument: curve fitting of the Si 2p core level. *Appl. Surf. Sci.*, **1999**, 137(1–4), 179–183.
54. Kou L., and Gao C., Making silica nanoparticle-covered graphene oxide nanohybrids as general building blocks for large-area superhydrophilic coatings. *Nanoscale,* **2011**, 3(2), 519–528.
55. Mayakrishnan G., Ick Soo K., and Ill Min C., Stepwise Construction of Ru(II)Center Containing Chiral Thiourea Ligand on Graphene Oxide: First Efficient, Reusable, and Stable Catalyst for Asymmetric Transfer Hydrogenation of Ketones. *Catalysts,* **2020**, 10(2), 175.
56. Shuai C., Yu L., Feng P., Zhong Y., Zhao Z., Chen Z., and Yang W., Organic montmorillonite produced an interlayer locking effect in a polymer scaffold to enhance interfacial bonding. *Mater. Chem. Front.*, **2020**, 4(8), 2398–2408.
57. Arjmandi R., Balakrishnan H. and Hassan A., Enhanced Flame Retardancy, Thermal and Mechanical Properties of Hybrid Magnesium Hydroxide/Montmorillonite Reinforced Polyamide6/Polypropylene, *Nanocomposites,* **2018,** 19, 914–926.
58. Wu W. and Yu B., Cornmeal Graphene/Natural Rubber Nanocomposites: Effect of

Modified Graphene on Mechanical and Thermal Properties., *ACS Omega*, **2020**, 15, 8551–8556.

59. Wei J., Saharudin M. S. and Vo T., Effects of surfactants on the properties of epoxy/ graphene nanocomposites. *SAGE,* **2018,** 14, 960–967.
60. Marcantonio E., Zanardi F., Curti C., & Lombardo M. Mechanistic Insights into the Stepwise (4+2) Cycloaddition toward Chiral Fused Uracil Derivatives. *Advanced Synthesis & Catalysis*, **2023**, 365, 1531–1539.